Interaction of a Dynamic Rupture on a Fault Plane with Short Frictionless Fault Branches

Ronald L. Biegel,[1] Charles G. Sammis,[1] and Ares J. Rosakis[2]

Abstract—Spontaneous bilateral mode II shear ruptures were nucleated on faults in photoelastic Homalite plates loaded in uniaxial compression. Rupture velocities were measured and the interaction between the rupture front and short fault branches was observed using high-speed digital photography. Fault branches were formed by machining slits of varying lengths that intersected the fault plane over a range of angles. These branches were frictionless because they did not close under static loading prior to shear rupture nucleation. Three types of behavior were observed. First, the velocity of both rupture fronts was unaffected when the fault branches were oriented 45° to the main slip surface and the length of the branches were less than or equal to ~0.75 R_0^* (where R_0^* is the slip-weakening distance in the limit of low rupture speed and an infinitely long slip-pulse). Second, rupture propagation stopped at the branch on the compressive side of the rupture tip but was unaffected by the branch on the tensile side when the branches were ~1.5 R_0^* in length and remained oriented 45° to the principle slip surface. Third, branches on the tensile side of the rupture tip nucleated tensile "wing tip" extensions when the branches were oriented at 70° to the interface. Third, when the branches were oriented at 70° to the interface, branches on the tensile side of the rupture tip nucleated tensile "wing-crack" extensions. We explain these observations using a model in which the initial uniaxial load produces stress concentrations at the tips of the branches, which perturb the initial stress field on the rupture plane. These stress perturbations affect both the resolved shear stress driving the rupture and the fault-normal stress that controls the fault strength, and together they explain the observed changes in rupture speed.

Key words: Fault mechanics, earthquakes, branching, shear rupture, fault rock, damage.

Introduction

A major challenge in earthquake mechanics is the development of a quantitative relation between fault mechanics and fault zone structure. From a fault mechanics perspective, an earthquake is a propagating rupture on an existing fault surface, which is controlled by sliding friction. Fracture energy is the work done in reducing the coefficient of friction from its static value to a lower dynamic one, this reduction requires a characteristic sliding displacement that occurs over a characteristic distance behind the crack tip (HUSSEINI *et al.*, 1975; RICE, 1980). Real faults, many exhumed

[1] Department of Earth Sciences, University of Southern California, Los Angeles, CA, 90089, U.S.A.
[2] Graduate Aeronautical Laboratories, California Institute of Technology, Pasadena, CA, 91125, U.S.A.

from seismogenic depths, have a more complex structure. Most of the displacement appears to have been accommodated in a narrow "core" (centimeters thick) of extremely fine-grained fragmented rock termed "ultracataclasite" (SIBSON, 2004; CHESTER *et al.*, 1993; SIMPSON, 1991). This ultracataclasite layer is often foliated and indurated, and sometimes contains one or more prominent slip surfaces that appear to have accommodated most of the displacement. The core is bordered by wider zones of fault gouge and breccia, typically meters thick with particle sizes ranging from microns to centimeters and often having a power-law size distribution (SAMMIS *et al.*, 1987). The gouge and breccia zones are bordered, in turn by fractured but cohesive wall rock in which the fracture density (damage) decreases to the regional background level over a distance of one to several hundreds of meters. There is a wide range of variation in this basic structure, particularly in the widths of the constitutive layers and in degree of symmetry about the core (see recent reviews by BEN-ZION and SAMMIS, 2003 and BIEGEL and SAMMIS, 2004).

Two key, and possibly related questions are: (1) How does fault zone structure form and (2) does this structure affect rupture propagation. In this paper we focus on the second question and, in specific, ask how short frictionless fault branches affect the rupture velocity on the main fault.

We define short branches as fractures that intersect the principal slip surface but are otherwise indistinguishable from the myriad of fractures that comprise a fault zone and are generally termed as "off-fault damage." Fault zone damage spans a wide range of sizes from nanometer scale in the core (CHESTER *et al.*, 2005) to branching cracks that can be many meters in length. If we view the boundaries between interlocked fragments as fractures, then all off-fault damage (including the fractured wall rock and short branches) can be viewed as an array of fractures and the interaction between these fractures and the crack tip stress field of an earthquake rupture can be calculated using standard fracture mechanics.

We expect this array of off-fault damage to affect rupture propagation in several ways. First, the elastic moduli of a rock massif are very sensitive to the density and size spectrum of its internal fractures (O'CONNELL and BUDIANSKY, 1974). In general, this has the effect of lowering the limiting rupture speed, and may even affect the direction of rupture propagation if the fracture-induced elasticity reduction is asymmetric about the fault plane. (DOR *et al.*, 2006).

If an earthquake causes the dynamic stress level in the fault zone to rise above the Coulomb criterion, then frictional sliding may occur on favorably oriented fractures, which can reduce energy flow to the crack tip and further slow propagation (ANDREWS, 2005; TEMPLETON *et al.*, 2006; VIESCA *et al.*, 2006). Even higher stress levels can nucleate additional cracks in the fault zone, thereby removing additional energy from the field.

At a larger scale, dynamic rupture calculations by BHAT *et al.* (2006) have shown that slip on finite fault branches as short as $\sim 6R_0$ can cause propagation on the main fault to pause or even stop where R_0 is the slip-weakening distance from POLIAKOV

et al. (2002). In the BHAT *et al.* (2006) simulations, the walls of the branches were in frictional contact with a coefficent of $\mu = 0.6$.

In this paper we present an experimental study of interaction between dynamic ruptures on a fault plane and short frictionless branches. The results of these experiments could apply to the special case where tectonic loading causes fluid pressures to reach lithostatic levels in a fault zone thus causing a low effective coefficient of friction on the intersecting fault branches. Alternatively, if thermal pressurization occurred during faulting then it could not only increase fluid pressures and reduce friction in the main fault zone but also on short branches.

Experimental Procedure

As a first step in our laboratory study of the effect of fault branches on dynamic rupture, we present here observations of the interaction of a dynamic rupture propagating along the interface between two photoelastic Homalite plates and isolated short branch faults. A high-speed digital camera was used to document the rupture propagation along the fault and its interaction with the short branches.

As shown in Figure 1, square photoelastic Homalite 100 plates (15.24 cm× 15.24 cm × 0.95 cm) were cut at an angle of 25° to form a fault as in XIA *et al.* (2004). Physical properties of Homalite 100 are given in Table 1. Fault surfaces were polished with 10 micron grit. Each sample had a 0.1-mm diameter hole at the center of the main fault into which a nickel chromium wire was inserted before the samples were placed into a loading frame.

The experimental apparatus in Figure 2, is a plane polariscope in which contours of equal shear stress appear as dark fringes in the sample. The laser emits a continuous collimated beam of 514-nm wavelength that passes through a polarizer and the sample. It then passes through another polarizer to a beam-splitting mirror serving two identical digital cameras. Each camera has 8 digital frames set to record one frame every $2\mu s$ although a few experiments were recorded at half that framing rate. The cameras were triggered by a 5 V electrical signal discharged at the same time as the high voltage charge (1.5 kV) that vaporized the wire and nucleated the rupture by reducing the normal stress along about 1 cm of the fault plane centered on the wire. The rupture tips could be identified in the photographic records as areas of intense fringe concentration (high shear stress) moving along the fault plane. Fringes associated with the shear wave could also be identified as circular segments centered on the explosion. Because of the radiation pattern, they are best observed in the maximum lobe of the S-wave pattern, which is at right angle to the fault plane.

At the start of each experiment the samples were loaded to a pre-selected uniaxial normal stress, usually 12 MPa (a few at 10 MPa or 15 MPa). The capacitor was then discharged to vaporize the NiCr wire and to simultaneously trigger the cameras.
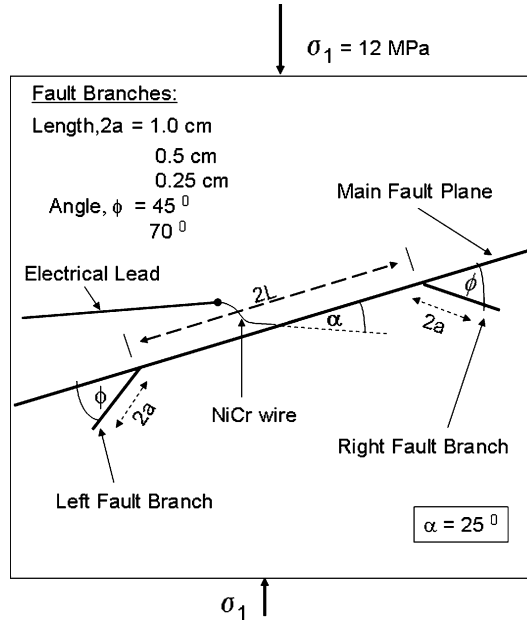
Figure 1

Sample geometry showing main fault and intersecting fault branches. The fault is at 25° to the horizontal and branches (slits) were cut at 45° or 70° to the fault. Rupture was nucleated by exploding a NiCr wire at the center of the fault. A compressive uniaxial load (typically 12 MPa) was applied to top and bottom of the sample.

After each experiment the decrease in uniaxial load was recorded and the sample removed for inspection.

We first tested samples without fault branches for comparison with XIA *et al.* (2004). We then introduced pairs of short branches, each of which was a slit about 1 cm or less in length that intersected the main fault. Branches in each pair were located at equal distances L from the nucleation point at the center of the fault plane

Table 1

Physical properties of Homalite 100. Elastic constants are from DALLY *and* RILEY *(1991). Static and dynamic friction constants are from* XIA *et al. (2004)*

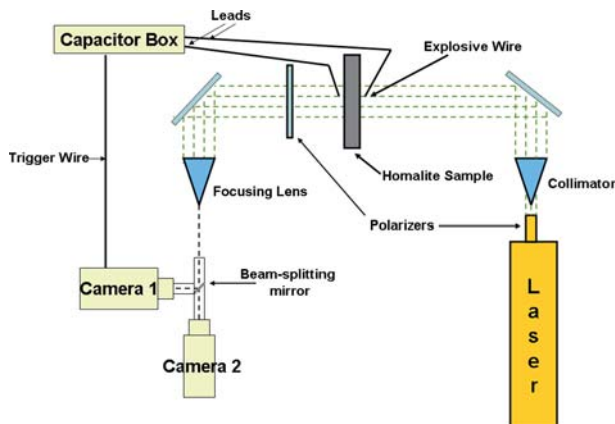|	
E, Young's Modulus (GPa)	3.9
μ, Shear Modulus (GPa)	1.4
v, Poisson's Ratio	0.35
f_s (static)	0.6
f_d (dynamic)	0.2

Figure 2

Diagram of the experimental apparatus. A high-speed digital camera capable of up to 10^8 frames sec^{-1} records transient fringes produced by a propagating dynamic rupture in photoelastic (Homalite) sample plates. A collimated laser source illuminates the fault system for the camera. A hydraulic press applies a uniaxial load to a fault oriented 65° to σ^1. A NiCr wire is inserted into a hole between the plates and vaporized by an electric discharge from the capacitor box. (Redrawn from XIA *et al.*, 2004).

and at angles of either 45° or 70° to the fault plane. The slits were 1.0 cm, 0.5 cm or 0.25 cm long and approximately 0.5 mm wide.

Experimental Results

The experimental conditions for 25 tests are given in Table 2, which is subdivided into four series of experiments depending on the experimental configuration and the nature of the observed interaction between the shear rupture and the fault branch.

Series 1—No Branches and sub-Rayleigh Rupture Velocity

For this series, no fault branches were present in the samples and the observed rupture speed was sub-Rayleigh. Figure 3(a) shows one of sixteen digital images taken during experiment C-13. The left and right propagating rupture tips are clearly visible along the interface and the circular shear-wave fringe can be identified. Figures 4(a) and 4(b) show the rupture length and the propagation distance of the maximum shear-wave fringe as functions of time. The speeds shown are comparable to those measured by XIA *et al.* (2004).

The error bars in Figures 4(a) and 4(b) and subsequent figures have values of ±1.5 mm, the estimated accuracy with which the position of the rupture tip and the maximum shear-wave peak could be measured in the digital images. The percent error in timing was much less and has been neglected. The shear-wave phase velocity
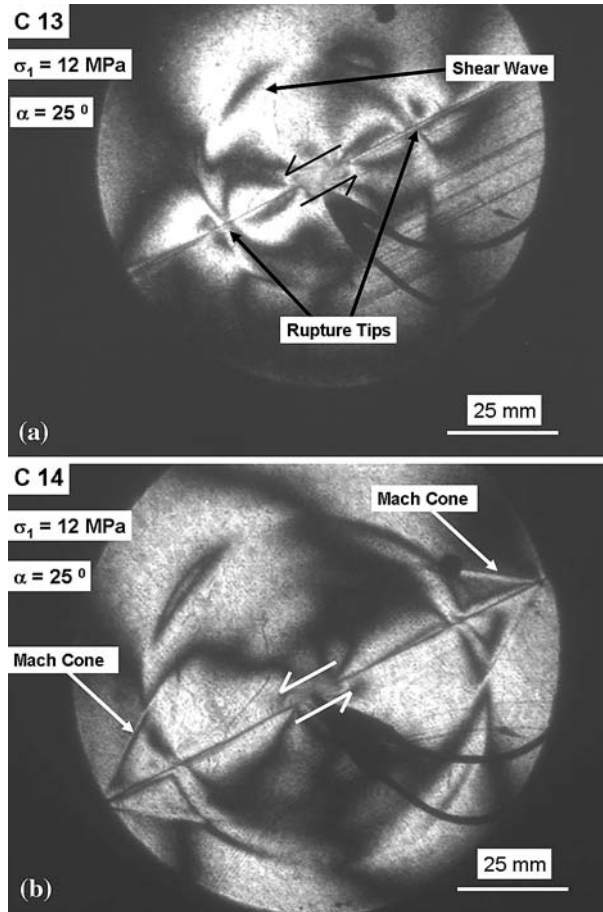
Figure 3

Panel (a) is a digital image from experiment C-13. Rupture tips from the bilateral rupture appear as dark points (shadow spots) propagating to the left and right along the fault from a central nucleation point. The shear wave can be most clearly seen propagating toward the upper left of the field of view. Panel (b) is a digital image from experiment C-14. The Mach cones to the left and right along the interface are characteristic of supershear rupture velocity.

was found by plotting a circle centered at the rupture nucleation point and passing through the center of the maximum shear wave fringes. Our reported errors in rupture and shear-wave speeds are the maximum and minimum slopes that lie within all the individual error bars.

Series 2—No Fault Branches and Supershear Rupture Propagation

The experimental conditions in Series 2 experiments were identical to those in Series 1 except the uniaxial load was slightly greater (with the exception of
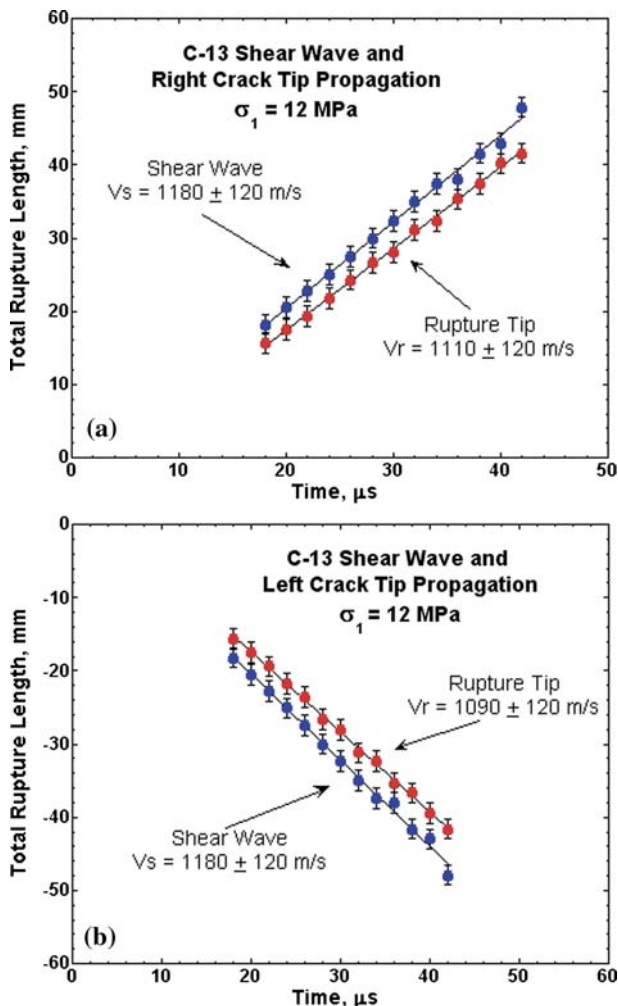
Figure 4
Rupture length versus time plots for experiment C-13. Panel (a) is for the right propagating rupture tip and shear wave, while panel (b) is for the left propagating rupture tip and shear wave. The error bars indicate a ± 3 mm uncertainty in picking the rupture front and shear wave. Uncertainties in speed are the maximum and minimum slopes allowed by the error bars.

experiment C-13). As discussed by XIA *et al.* (2004), an increase in normal stress decreases the transition length to supershear and allows observation of this phenomenon within the field of view of the camera system.

The Mach cones visible in Figure 3(b) (experiment C-14) are characteristic of supershear rupture (for more information on shear Mach cone formation see ROSAKIS *et al.* (1999), SAMUDRALA *et al.* (2002), XIA *et al.* (2004), and DUNHAM

Table 2

Table of experiments classified by geometrical configuration and the nature of the interaction between the shear rupture and the intersecting fault branches. The columns give experiment name, normal load before the experiment, σ_1, and normal load after the experiment, σ'_1. Note, the normal load shown is the remote uniaxial load, not the normal stress resolved onto the main fault

Table of Experiments		
Experiment	σ_1, MPA	σ'_1, MPA
Series 1 - No Fault Branches, Sub-Rayleigh Rupture Velocity		
C5	9	8.9
C6	9	8.0
C7	10	7.8
C8	10	7.8
C9	10	6.0
C10	10	7.8
C11	10	7.5
C13	12	11.5
Series 2 - No Fault Branches, Supershear Rupture Velocity		
C12	12	9.0
C14	12	10.3
Series 3 - Fault Branches, No Crack Extension		
1.0 cm slits, 45° from fault		
C15	12	10.6
C16	12	7.8
C17	15	13.0
C18	15	13.6
C19	15	15.0
C20	15	15.0
C21	12	10.2
C25	12	11.2
C27	12	11.6
0.5 cm slits, 45° from fault		
C22	12	10.2
C23	12	10.2
C28	12	—-
C29	12	10.8
0.25 cm slits, 70° from fault		
C30 4 slits	12	—
C32	12	12
C33	12	12
C34	12	12
C35 4 slits	12	12
Series 4 - Fault Branches with Crack Extension		
0.5 cm slits, 45° from fault		
C24	12	11
C26	12	10.9
0.25 cm slits, 70° from fault		
C31 4 slits	12	9.6
		2.5 cm crack

(2006)). Note in Table 2 that the uniaxial load of 12 MPa in both C-13 and C-14 is very near the value at which supershear propagation becomes observable. The smaller drop in uniaxial stress observed in experiment C-13 probably reflects a difference in the fault surface for that experiment, and may explain why the rupture speed remained sub-Rayleigh in the field of view of that experiment.
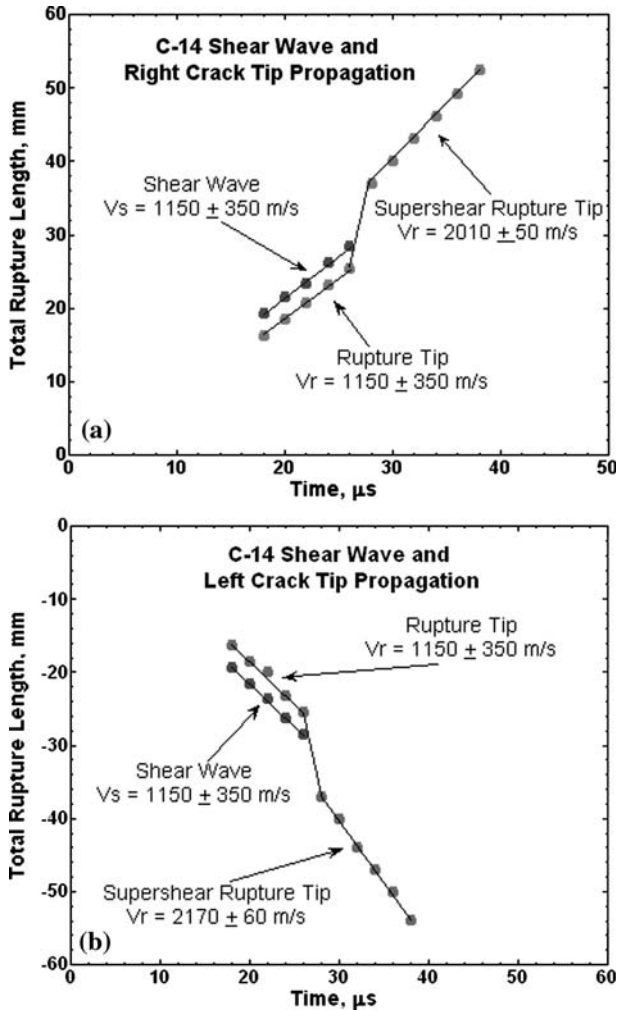

Figure 5
Rupture length versus time plots for experiment C-14. Panel (a) is for the right propagating rupture tip and shear wave, while panel (b) is for the left propagating rupture tip and shear wave. The supershear velocities were calculated from the Mach cone angle δ where $(V_r/V_s = 1/\text{sine } \delta)$. The transition to supershear occurred about 24µs to 30µs after nucleation for both rupture tips.

Figures 5(a) and 5(b) are rupture length versus time curves for the right and left propagating tips in experiment C-14. After about 25 mm of sub-shear propagation the rupture speed transitioned to a supershear speed of about 86% to 89% of the P wave speed in good agreement with XIA *et al.* (2004). Note that $V_r = \sqrt{2}V_s$ within measurement errors as expected (ROSAKIS, 2003).

Series 3—Fault Branches with no Tensile Wing-cracks

Series 3 samples had either two or four fault branches (slits at an angle $\Psi = 45°$ to the fault plane) in the lower plate (except for C-15 and C-16 which also had branches in the upper plate). This series has been divided into two parts: Series 3-A where the branches were slits of length $2a = 1$ cm, and rupture propagation was stopped by one or more branches, and Series 3-B where the slits were shorter ($2a = 0.5$ cm and 0.25 cm) and rupture was not stopped by either branch. Mode I crack growth into the intact Homalite did not nucleate at the tips of the branches in either series.

Figure 6(a) shows a frame from experiment C-17 (Series 3-A), which has two slits intersecting the lower side of the fault at points equidistant from the nucleation point. Note the stress concentration at the left rupture front has extended beyond the left fault branch and is propagating at supershear speed as evidenced by the Mach cone. However, the right rupture front is no longer visible, having terminated at the right slit. Figures 7(a) and 7(b) are the rupture length versus time plots for C-17. On the right side of the nucleation point the rupture front was observed to stop when it interacted with the slit. This is evident in Figure 7(a) where $v_r \approx 0$ beyond the point (about 30 mm from the nucleation point) where the compressional side of the rupture interacted with the branch. Figure 7(b) shows no change in initial rupture speed as the tensile side of the rupture interacted with the element. The only effect of the slit was to delay the transition to supershear, which became possible after the rupture tip had moved away from the stress field of the slit. This delay is obvious if one compares Figures 5(b) and 7(b). The new transition length, L_d, with the fault branch present is approximately equal to $L_d \approx 50$ mm, as opposed to $L_d \approx 25$ mm without the branch present.

In Series 3-B where $2a = 0.5$ cm, the rupture continued to propagate past the fault branches on both sides of the nucleation point (see Figs. 6 (b), 8 (a) and 8 (b)). What is noteworthy in this case is that the interaction of both rupture tips and branches affected the rupture speeds in the sense that neither tip transitioned to supershear within the field of observation.

Series 4—Fault Branches with Tensile Wing-cracks

Series 4 consisted of three experiments in which additional damage nucleated within the tensile lobe of the propagating rupture in the form of Mode I tensile wing cracks extending from the branches in the lower plate. Two experiments, C-24 and C-26 (2 slits each) had wing crack extensions a few mm in length. Experiment
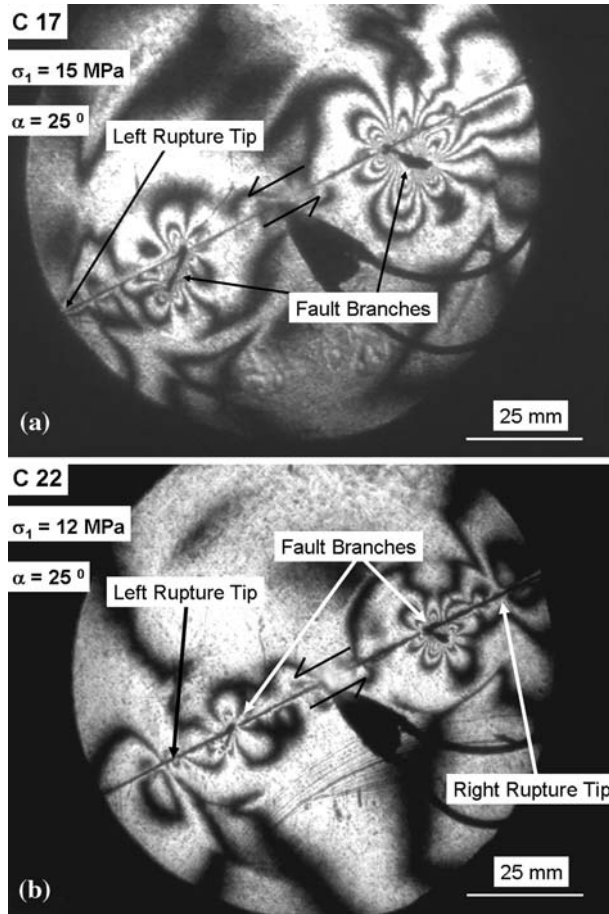
Figure 6
Panel (a) is a digital image from experiment C-17. The left rupture tip has passed the left branch and gone super-shear as indicated by the Mach cone, but the right tip cannot be seen because it was stopped by the right branch. Panel (b) is a digital image from experiment C-22. The rupture tips can be clearly seen to have passed their respective fault branches.

C-31 (Figs. 9 (a, b)) had 2 left and 2 right slits. The sample nucleated a crack about 2.5-cm long on the inner left slit and a few mm long from the outer left slit. There are two possible ways that these wing cracks could have nucleated: 1) The tensile field of the main rupture caused the branch to extend in tension or 2) shear displacement on the main fault jumped to the branch and this shear displacement nucleated a wing crack by the mechanism described in ASHBY and HALLAM (1986). The first possibility is suggested by the fact that the branches are nearly parallel to the uniaxial loading stress (vertical), which is the preferred propagation direction of a wing crack nucleated by the stress field of the main rupture. The second
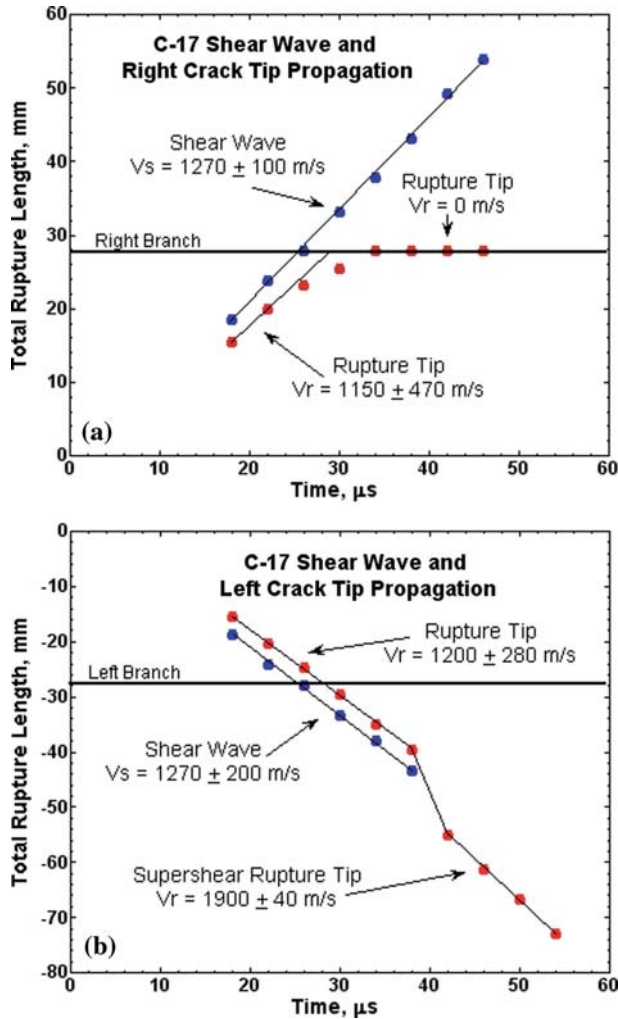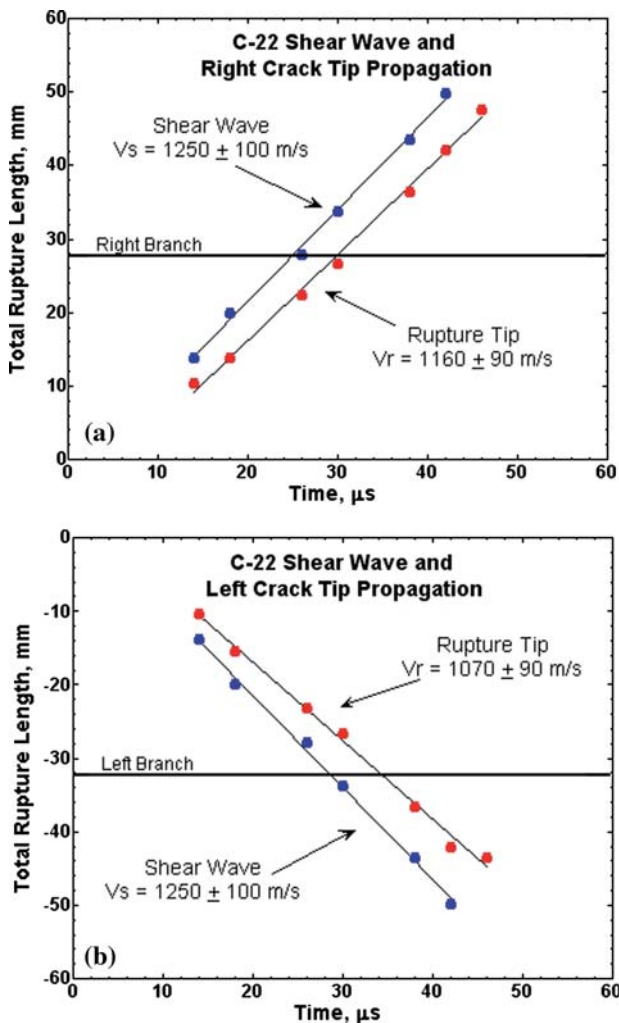
Figure 7

Rupture length versus time plots for experiment C-17. Panel (a) is for the right propagating rupture tip and shear wave, while panel (b) is for the left propagating rupture tip and shear wave. Note that the right propagating rupture tip stops at the intersecting branch indicated by the horizontal line while the left propagating tip is unaffected by the left branch and transitions to supershear propagation. The supershear velocity was calculated from the Mach cone angle, δ where ($V_r/V_s = 1/\text{sine } \delta$).

mechanism is suggested by the fact that the angle between the branch and the fault plane is 70°, which is near the optimal angle for branching (KAME *et al.*, 2003). This second mechanism is also supported by the geometry of the wing crack in Figure 9(b), where it is observed to nucleate at a high angle to the slit before curving to become more parallel to σ_1. This is the expected geometry if the wing

Figure 8
Rupture length versus time plots for experiment C-22. Panel (a) is for the right propagating rupture tip and shear wave, while panel (b) is for the left propagating rupture tip and shear wave. Note that the right and left propagating tips are unaffected by their respective branches.

crack is nucleated by shear displacement on the branch and not by its simple extension in tension (ASHBY and HALLAM, 1986). If the branch were instead an infinitely long fault, slip would have mostly transferred to that fault. For the finite length branch, this diversion ended in the nucleation and growth of a tensile wing crack. The weakened pulse on the main fault was only able to nucleate a much smaller wing crack at the second slit.
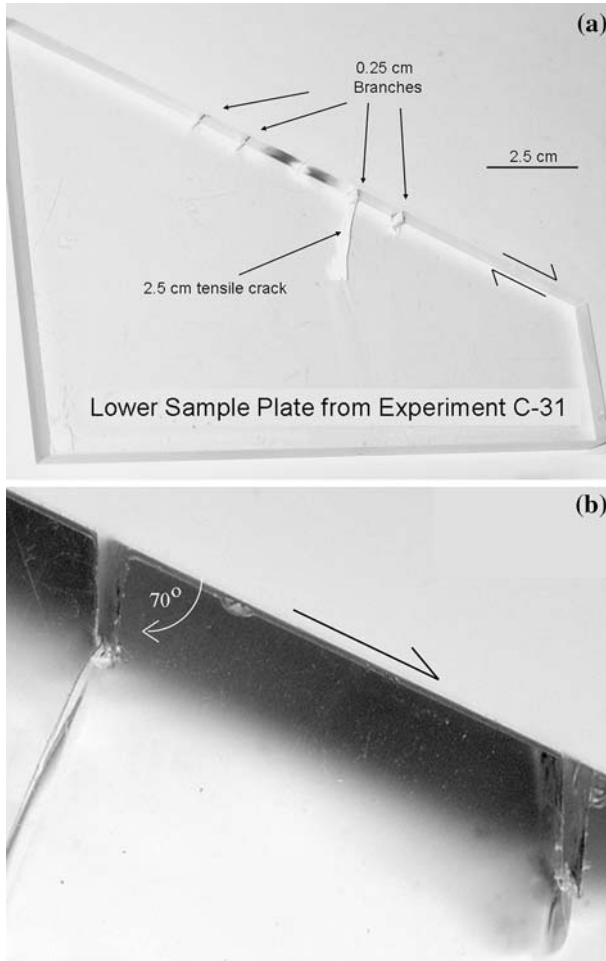
Figure 9
Lower half of sample from experiment C-31. Four fault branches were cut into this sample, 2 to the left of the nucleation center and 2 to the right. (a) Image of entire plate showing mode I crack growth from the inner right branch. Crack growth of the outer right slit was about 0.25 mm. No Mode I cracks nucleated from the left fault branches. (b) Close up of C-31 sample plate. Mode 1 crack growth is clearly visible.

Experimental Interpretation

There are at least two ways in which our simulated fault branches could affect the speed of a rupture propagating on the main fault. First, if the initial load had actually closed the branches then lateral shearing of the contacting sides caused by off-fault stresses from the passing rupture could produce a frictional energy loss, which would lower the rupture speed along the main fault. However, this mechanism can be ruled

out in the present study where the maximum closure for the fault branches is significantly less than their width. The maximum closure is given by

$$w_{\max} = \sigma_n(2a/E), \qquad (1)$$

where σ_n is the stress normal to the slit, $2a$ is the slit length, and E is Young's Modulus. For Homalite 100, the material properties in Table 1 yield $\Delta w_{\max} < 40$ μm, much less than the $500\mu m$ pre-load width of the branches. The fault branches are thus "frictionless" in all experiments in this paper.

A second hypothesis is that initial pre-load produces stress concentrations at the ends of the intersecting branches, which change both the normal and resolved shear stress on the fault planes and either slow down or accelerate the rupture. These stress concentrations can be seen in Figure 10, which is a photograph of the isochromatics recorded for sample C-22 after loading but before detonation of the NiCr wire. Note the pre-existing maximum shear stress fringes around the branches.

To explore this hypothesis further, we calculated the stress field perturbations resulting from the loaded branches (slits), and then inferred the changes these perturbations caused to normal and resolved shear stresses along the rupture interface.

We begin by following the analysis in ASHBY and HALLAM (1986), to calculate the "effective shear stress" produced by the initial uniaxial load σ_1 on the fault branches. [Here we perform a quasi-static analysis because the "effective shear stress" is applied by the uniaxial loading but prior to rupture nucleation. For a dynamic analysis, see
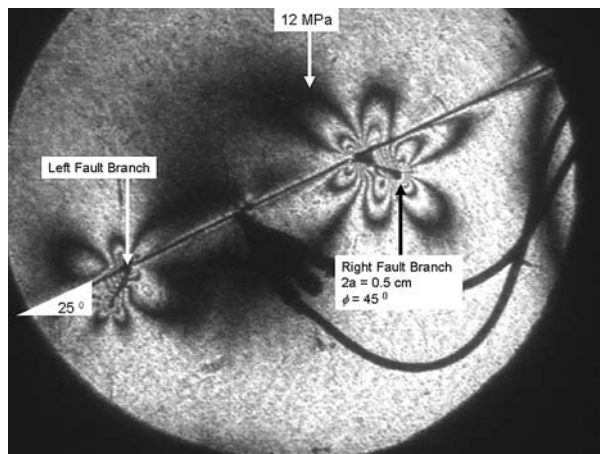

Figure 10
Digital image of a sample loaded to 12 MPa prior to nucleation. Note the butterfly fringes surrounding the right and left intersecting fault branches. Fringe patterns around the right branch are more pronounced because the right branch has undergone more shear slip.
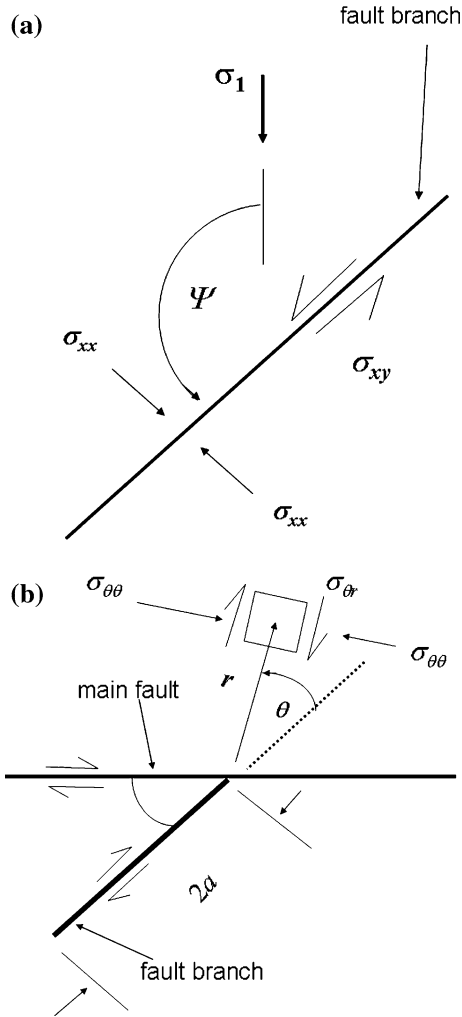
Figure 11

(a) Loading geometry for a fault branch at an angle Ψ to σ_1. σ_{xx} and σ_{xy} are the normal and shear stresses on the branch. (b) Definition of stresses $\sigma_{\theta\theta}$ and $\sigma_{\theta r}$ at distance r and angle θ from the crack tip of a fault branch. Note that $\sigma_{\theta\theta}$ is the normal stress and $\sigma_{\theta r}$ is the shear stress on the fault plane which makes an angle θ with the branch.

RICE (1980), FREUND (1990), and POLIAKOV *et al.* (2002).] The resolved normal and shear stresses in a plane occupied by a branch are given by

$$\frac{\sigma_{xx}}{|\sigma_1|} = \frac{1}{2}(1 - \cos 2\psi) \quad \text{and} \quad \frac{\sigma_{xy}}{|\sigma_1|} = -\frac{1}{2}\sin 2\psi, \tag{2}$$

where ψ is the angle between the branch direction and the loading axis as illustrated in Figure 11(a). Note that (x, y) are in the coordinate system of the fault branches.

The effective shear stress on any branch is then given by

$$\frac{\sigma'_{xy}}{|\sigma_1|} = \left|\frac{\sigma_{xy}}{\sigma_1}\right| + f_s \frac{\sigma_{xx}}{\sigma_1}, \tag{3}$$

where σ_{xx} is always positive, f_s is the static coefficient of friction and, if $|\sigma_{xy}| \leq |f_s\sigma_{xx}|$, then $\sigma'_{xy} = 0$.

The stress intensity factor at the tips of a fault branch of length $2a$ is therefore

$$K_{II} = \sigma'_{xy}\sqrt{\pi a}, \tag{4}$$

while the stress field near the tips of the branches can be written in terms of K_{II} as

$$\sigma_{\theta\theta} = \frac{K_{II}}{\sqrt{2\pi r}}F_{\theta\theta}^{II} \quad \text{and} \quad \sigma_{\theta r} = \frac{K_{II}}{\sqrt{2\pi r}}F_{\theta r}^{II}, \tag{5}$$

where the geometrical factors are

$$F_{\theta\theta}^{II} = -\sin\frac{\theta}{2} \bullet 3\cos^2\frac{\theta}{2} \quad \text{and} \quad F_{\theta r}^{II} = \cos\frac{\theta}{2}\left(1 - 3\sin^2\frac{\theta}{2}\right). \tag{6}$$

The (r, θ) coordinate system is defined relative to the fault branch as shown in Figure 11(b).

Substituting eqn. (4) into (5) gives, in dimensionless form,

$$\frac{\sigma_{\theta\theta}}{|\sigma_1|} = \sqrt{\frac{a}{2r}}\frac{\sigma'_{xy}}{|\sigma_1|}F_{\theta\theta}^{II} \quad \text{and} \quad \frac{\sigma_{\theta r}}{|\sigma_1|} = \sqrt{\frac{a}{2r}}\frac{\sigma'_{xy}}{|\sigma_1|}F_{\theta r}^{II}. \tag{7}$$

For our experiments, $f_s = 0$ and eqns. (7) can be simplified to

$$\frac{\sigma_{\theta\theta}}{|\sigma_1|}\sqrt{\frac{2r}{a}} = \left(\frac{\sin 2\psi}{2}\right)\left(-\sin\frac{\theta}{2}\right)\left(3\cos^2\frac{\theta}{2}\right) \tag{8}$$

and

$$\frac{\sigma_{\theta r}}{|\sigma_1|}\sqrt{\frac{2r}{a}} = \left(\frac{\sin 2\psi}{2}\right)\left[\cos\frac{\theta}{2}\left(1 - 3\sin^2\frac{\theta}{2}\right)\right]. \tag{9}$$

Note in Figure 11(b) that θ or $\pi - \theta$ is the angle ϕ between the plane of the branch and the fault plane, so $\sigma_{\theta\theta}$ is the change in normal stress on the fault plane and $\sigma_{\theta r}$ is the change in shear stress caused by the loaded branch, both at a distance r from the tip of the branch.

Figure 12(a) displays normalized stress components from eqns. (8) and (9) for the left side (upper graph) and right side (lower graph) of the right fault branch. Values of ϕ vary from 0 to 90° where ϕ is the angle of the element from the main fault (see
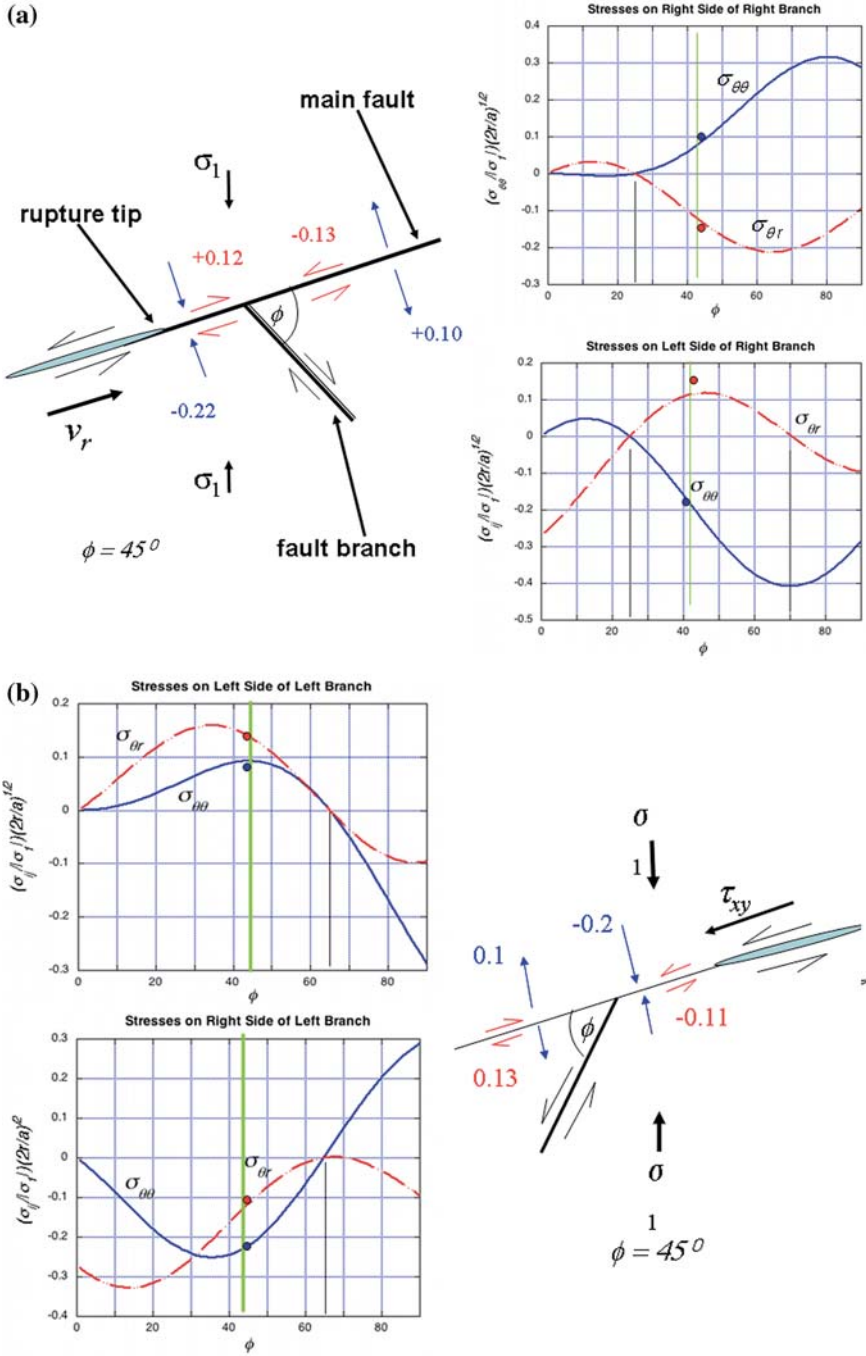
(a)

(b)

◄
Figure 12

Shear and normal stress changes along the main fault near the branches. Panel (a) shows stresses on the fault plane near the right element. The two graphs in Panel (a) show normal and shear stresses on either side of the branch for any intersection angle ϕ. The diagram shows the special case for $\phi = 45°$. Changes in normal and shear stress on the fault plane are indicated, positive numbers assist the left lateral rupture while negative numbers retard it. Panel (b) contains the same information as Panel a, except it is for the left fault branch.

Fig. 1). The vertical lines on the upper and lower graphs indicate the values of the normalized stress perturbations $\sigma_{\theta r}$ and $\sigma_{\theta\theta}$ along the rupture interface for a branch oriented 45° from the main fault.

The magnitudes of these stresses are shown in the drawing to the left of the graphs in Figure 12(a). A left lateral rupture is shown approaching a fault branch. On the left side of the element the normal stress change on the rupture interface is $-0.22|\sigma_1|$ (at a distance of $r = a/2$ along the fault plane from the intersection with the branch) indicating increased normal compression. Additionally, the branches generates a shear stress of $+0.12|\sigma_1|$ right lateral) on the fault plane. Hence both stress perturbations on the fault plane resist propagation of the left lateral advancing rupture. The resisting stress is proportional to the far field uniaxial load σ_1.

If the rupture is not stopped by these stress perturbations, its propagation on the right side of the branch is temporarily enhanced by a reduction in the normal stress and a left lateral shear stress. On this side of the element the rupture is likely to accelerate.

Stress perturbations at the left fault branch are shown, in the same format, in Figure 12(b). As the left lateral rupture approaches the left branch its propagation is enhanced by a left lateral shear perturbation but opposed by increased normal stress. Once past the left branch the rupture encounters tensional normal force changes that enhance propagation, and right lateral shear stresses that oppose it. The net effect seems to be little or no change in rupture velocity at the left branch, as observed.

Coulomb stress is defined as $C = |\sigma_{\theta r}| - f_s|\sigma_{\theta\theta}|$. Hence $C = 0$ marks the onset of frictional sliding where negative values C correspond to a frictionally locked surface while positive values of C imply sliding. An increase in $C(\Delta C > 0)$ enhances frictional sliding while a decrease ($\Delta C < 0$) suppresses sliding. Figure 13(a) shows the magnitude of the local Coulomb stress changes for a sample interface with the fault branch oriented at 45°. The Coulomb changes from the perturbations are normalized by C_0 the Coulomb stress on an interface in the absence of any fault branches. We see that the right branch generates Coulomb stress changes several times greater than those on the left side of the interface. We argue that this is the reason the right branch was observed to stop the right rupture propagation while the left branch did not.

Figure 13(b) shows Coulomb stress changes along a fault plane with branches at a 70° angle from it. Note that the stresses have changed from Figure 12(a) in a way
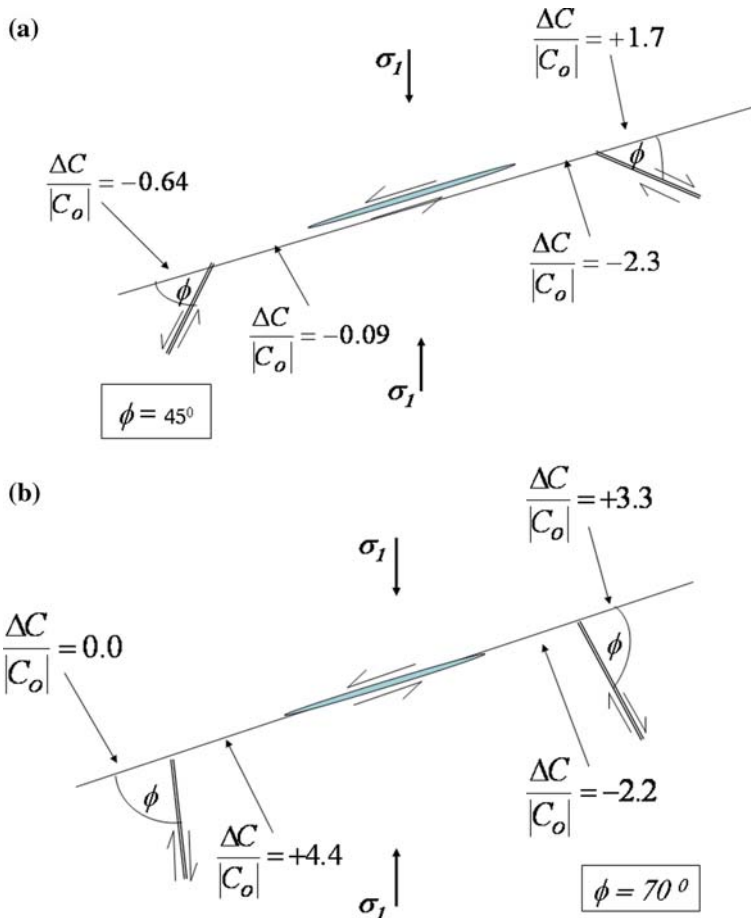
Figure 13
Change in Coulomb stress on the fault plane near 1.0 cm long fault branches. All values are normalized to C_0, the Coulomb stress on the fault plane after loading but before nucleation. Panel (a) is the case for $\phi = 45°$ while Panel (b) is for $\phi = 70°$. Positive changes in Coulomb stress moves the fault closer to failure.

that makes it more likely that the rupture will be stopped by the right side fault branch, but less likely it will be stopped by the branch on the left side.

Finally we note that equations (8) and (9) have a term $1/\sqrt{a}$ where a is half the branch length. This means longer frictionless branches generate larger stress perturbations and Coulomb stress changes. Table 2 shows that all intersecting fault branches with lengths of 1.0 cm stopped right rupture propagation at the right branch. All samples with branches of 0.5 cm and 0.25 cm did not stop right propagation.

Scaling from the Laboratory to the Field-R_0^*

We have shown in our experiments that a rupture can be slowed or stopped by short (1 cm) frictionless branches. The question naturally arises, how does a 1 cm slit in our experiments compare to a real fault branch? To answer this question, we scaled our results to real faults using the analytical slip pulse model formulated by RICE *et al.* (2005). In a slip pulse, slip weakening occurs over a distance R behind the rupture front while active slip is restricted to a finite distance L. This model probably gives a good description of our experiments since ROSAKIS *et al.* (2006) have observed slip pulses in Homalite plates under the loading conditions in our experiments. RICE *et al.* (2005) give analytical expressions for the stress field near the tip of a propagating mode II (or mode III) slip pulse in dimensionless form, where lengths are scaled by R_0^*, the value of R in the limit of low rupture speed, and an infinitely long slip pulse (Fig. 14a). This scaling length is given by
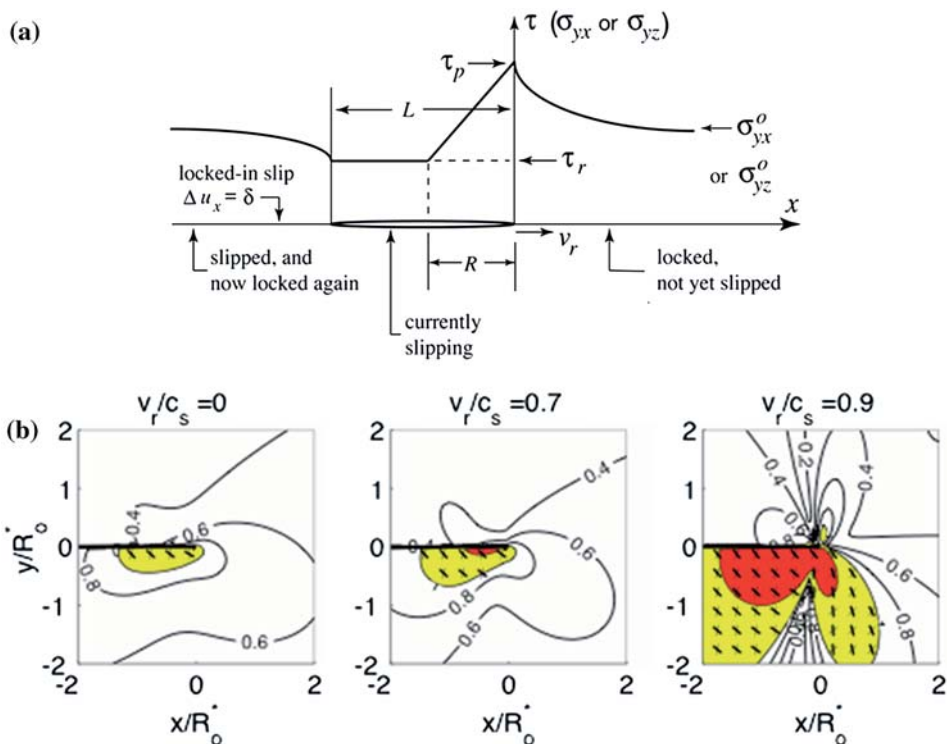

Figure 14
(a) Slip pulse of length L and slip weakening distance R propagating with speed v_r (from RICE *et al.*, 2005). (b) Spatial extent of off-fault stresses predicted by the RICE *et al.* (2005) slip pulse model. Note that length is scaled by R_0^*. Rupture speed is increasing from left to right.

$$R_0^* \approx \frac{9\pi}{16(1-v)}\frac{\mu\delta_1}{f_s\sigma_n}, \tag{10}$$

where μ is the shear modulus, f_s is the coefficient of friction, δ_1 is the characteristic displacement, and σ_n is the normal stress.

RICE *et al.* (2005) fit their model to data from HEATON (1990) and estimated R_0^* for several large earthquakes to be in the range 1.3 m to 36 m. Using the material properties of Homalite 100 from Table 1 and our experimental conditions in eqn. (10) we estimate $R_0^* \approx 6.5$ mm in our experiments. The large difference in R_0^* between Homalite and real faults is due mainly to the larger elastic constant in rock. Accordingly, a 1.0 cm slit in a Homalite sample corresponds to about a 2 m to 56 m branch on a real fault. The shorter branches in this range might be viewed as fractures within the fault zone—the longer ones as short fault branches.

Note in Figure 14(b) that the stress field is sensitive to the rupture velocity v_r. In most of our experiments v_r was near the Rayleigh wave speed 0.92 c_s so that the rightmost panel best represents the stress state near the fault in our experiments.

Discussion

Our experiments show that rupture propagation can be slowed or stopped by local stress perturbations produced by short frictionless branches on the main fault. These branches can also lengthen or shorten the transition length to supershear. Our observations suggest that short branches extending from a main fault may be a physical mechanism for "fault barriers" discussed by AKI (1979) and which seismologist have postulated to explain velocity fluctuations in ruptures (HUSSEINI *et al.*, 1975; PAPAGEORGIOU, 2003). Recent calculations by BHAT *et al.* (2006) suggest that branches with friction produce results similar to ours, but they require longer branches of scaled length $> 6R$ to slow or stop a dynamic rupture. We observed an equivalent reduction of the rupture speed for "frictionless" branches with a scaled length near R_0^* (~ 1 cm in our experiments).

The nucleation of off-fault damage as tensile wing-cracks is significant because it shows that dynamic rupture can activate the damage mechanics mechanism proposed by ASHBY and SAMMIS (1990). Since the spatial extent of off fault Coulomb slip ($\sim Ro^*$) was less than 1 cm in our experiments, it was difficult to fully explore this mechanism. When scaled up to real fault zones, the nucleation of such off-fault damage could provide the nonlinear relaxation postulated by the ANDREWS (2005) continuum model. However, it remains to be experimentally demonstrated that an array of frictional fault branches and off fault fractures can be sufficiently activated by a dynamic rupture to provide enough nonlinear strain to affect rupture velocity.

Acknowledgement

REFERENCES

AKI, K. (1979), *Characterization of barriers on an earthquake fault*, J. Geophys. Res. *84*, 6140–6148.

ANDREWS, D.J. (2005), *Rupture dynamics with energy loss outside the slip zone*, J. Geophys. Res. *110*, B01307, doi: 10.1029/2004JB003191.

ASHBY, M.F. and HALLAM, S.D. (1986), *The failure of brittle solids containing small cracks under compressive stress states*, Acta Metall. *34*, 497–510.

ASHBY, M.F. and SAMMIS, C.G. (1990), *The damage mechanics of brittle solids in compression*, Pure Appl. Geophys. *133*, 489–521.

BEN-ZION, Y. and SAMMIS, C.G. (2003), *Characterization of fault zones*, Pure Appl. Geophys. *160*, 677–715.

BHAT, H.S., OLIVES, M., DMOWSKA, R., and RICE, J. R. (2007), *Role of fault branches in earthquake rupture dynamics*, J. Geophys. Res., in press.

BIEGEL, R. and SAMMIS, C.G., *Relating fault mechanics to fault zone structure*. In *Advances in Geophysics*, Vol. 47 (ed. Dmowska, R.) (Elsevier, San Diego 2004), pp. 65–111.

CHESTER, J. S., CHESTER, F. M., and KRONENBERG, A. K. (2005), *Fracture surface energy of the punchbowl fault, San Andreas system*, Nature *437*, 133–136.

DOR, O., ROCKWELL, T. K., and BEN-ZION, Y. (2006), *Geologic observations of damage asymmetry in the structure of the San Jacinto, San Andreas and Punchbowl Faults in Southern California: A possible indicator for preferred rupture propagation direction*, Pure Appl. Geophys. *163*, 301–349, doi: 10.1007/s00024-005-0023-9.

DUNHAM, E. M. (2007), *Conditions governing the occurrence of supershear ruptures under slip-weakening friction*, J. Geophys. Res., in press.

HEATON, T. H. (1990), *Evidence for and implications of self-healing pulses of slip in earthquake rupture*, Earth Planet. Int. *64*, 1–20.

HUSSEINI, M.J., DUSHAN, B., JOVANOVICH, M.J., RANDALL, M.J., and FREUND, L.B. (1975), *The fracture energy of earthquakes*, Geophys. J. R. Astr. Soc. *43*, 367–385.

KAME, N., RICE, J.R., and DMOWSKA, R. (2003), *Effects of prestress and rupture velocity on dynamic fault branching*, J. Geophys. Res. *108*(B5), 2265, doi: 10.1029/2002JB002189.

O'CONNELL, R. J. and BUDIANSKY, B. (1974), *Seismic velocities in dry and saturated cracked solids*, J. Geophys. Res. *79*, 5412–5426.

PAPAGEORGIOU, A. (2003), *The barrier model and strong ground motion*, Pure Appl. Geophys. *160*, 603–634.

RICE, J. R. (1980). *The Mechanics of Earthquake Rupture*. In *Physics of the Earth's Interior*, (eds. A. Dzjewonski and E. Boschi), Proc. Internat. School of Physics, Enrico Fermi.

RICE, J.R., SAMMIS, C.G., and PARSONS, R. (2005), *Off-fault secondary failure induced by a dynamic slip-pulse*, Bull. Seismol. Soc. Am. *95*, 109–134, doi: 10.1785/0120030166.

Rosakis, A. J., Lu, X., and Lapusta, N. (2006), *Laboratory observations of crack-like and pulse-like ruptures*, EOS, Trans. Am. Geophys. Union, 87, (52), Fall Meet. Suppl., Abstract, S52B-07.

Rosakis, A.J. (2003), *Intersonic ruptures and the story of the square root of two times the S-wave speed, Symp. Dynamic Failure and Thin Film Mechanics honoring Professor L. B. Freund of Brown University on the Occasion of his 60th Birthday*, California Institute of Technology, Pasadena, California, January 16–18, 2003.

Rosakis, A.J., Samudrala, O., and Coker, D. (1999), *Cracks faster than the shear wave speed*, Science *284*, 1337–1340.

Sammis, C.G., King, G.C.P., and Biegel, R.L. (1987), *The Kinematics of Gouge Deformation*, Pure. Appl. Geophys. *125*, 777–812.

Samudrala, O., Huang, Y., and Rosakis, A.J. (2002), *Subsonic and intersonic shear rupture of weak planes with a velocity weakening cohesive zone*, J. Geophys. Res. *107*, B8, 10.1029/2001JB000460.

Sibson, R. H. (2003), *Thickness of the seismic slip zone*, Bull. Seismol. Soc. Am. *93*, 1169–1178.

Simpson, C. (1991), *A Reinterpretation of the Timing, Position, and Significance of Part of the Sacramento Mountains Detachment Fault, Southeastern, California*, Geol. Soc. Am. Bull. *103*, 751–761.

Templeton, E. and Rice, J. R. (2006), *Extent and distribution of off-fault plasticity during seismic rupture including bimaterial effects*, EOS, Trans. Am. Geophys. Union *87*, (52), Fall Meet. Suppl., Abstract, S34A-01.

Viesca, R. C., Templeton, E. L., Bhat, H. S., and Rice, J. R. (2006), *Pore fluid pressurization effects on earthquake rupture propagation with inelastic off-fault response*, EOS, Trans. Am. Geophys. Union *87*, (52), Fall Meet. Suppl., Abstract, S42A-04.

Xia, K., Rosakis, A.J., and Kanamori, H. (2004), *Laboratory earthquakes: The sub-Rayleigh-to-supershear rupture transition*, Science *303*, 1859–1861.

To access this journal online:
www.birkhauser.ch/pageoph